Chemical Science

ROYAL SOCIETY OF CHEMISTRY

EDGE ARTICLE

View Article Online
View Journal | View Issue

Cite this: *Chem. Sci.*, 2025, **16**, 16321

All publication charges for this article have been paid for by the Royal Society of Chemistry

Received 17th April 2025
Accepted 1st August 2025

DOI: 10.1039/d5sc02818c

rsc.li/chemical-science

Stabilizing NiFe active sites using a high-valent Lewis acid for selective seawater oxidation

Chenxi Liu,[a] Zefeng Teng,[a] Xu Liu,[a] Rui Zhang,[a] Jingqi Chi, *[a] Jiawei Zhu,[d] Junfeng Qin,*[b] Xiaobin Liu,[a] Zexing Wu [ac] and Lei Wang *[ac]

Seawater electrolysis for hydrogen production harnesses renewable energy sources, contributing to sustainable development. However, competing anodic reactions, such as the chloride oxidation reaction (ClOR), can adversely affect the activity and stability of the oxygen evolution reaction (OER). In this study, we propose a strategy that significantly enhances the OER activity and selectivity of NiFe-layered double hydroxides (LDHs) by incorporating chromium (Cr) (Cr-NiFeLDHs). The Cr-NiFeLDH anode demonstrates an impressive overpotential of only 349 mV at a current density of 1000 mA cm^{-2}, outperforming RuO_2 in industrial applications and maintaining stability for over 140 h in anion exchange membrane (AEM) electrolyzer tests. Quasi *in situ* characterization reveals that Cr doping activates the high valence states of Ni, Fe and Cr, enhancing the electron transfer and activity of OER performance. Furthermore, the high selectivity for OH^- due to the hard Cr^{6+} Lewis acid effectively mitigates the competitive ClOR, a critical challenge in seawater electrolysis. This synergistic stabilization effect of high valence states fundamentally enhances the activity, selectivity, and stability of Cr-NiFeLDH anodes.

Introduction

The electrolysis of water for hydrogen production offers several advantages, including environmental protection, ease of operation, and high efficiency. Despite this, most industrial electrolysis systems currently utilize pure water as the electrolyte, largely overlooking seawater, which comprises more than 97% of the Earth's water resources. Seawater presents a promising feedstock for electrolysis due to its superior reserves and distribution compared to pure water.[1–3] Similar to pure water electrolysis, the anodic oxygen evolution reaction (OER) significantly limits the widespread application of seawater electrolysis due to its low efficiency. More seriously, the competitive adsorption of OH^- and Cl^- at the anode during oxidation triggers the chloride oxidation side reaction (ClOR), which prevents the selective OER and hampers the electrolysis process.[4–6] The complete corrosion due to the formation of hypochlorite can lead to a cessation of hydrogen production at the cathode, ultimately resulting in electrolysis failure. While seawater electrolysis technology presents an attractive method for hydrogen production, it necessitates the development of an anode catalyst with selective active sites that can operate effectively and durably in Cl^- rich environments.

Currently, noble metals are considered ideal for the OER due to their high electrical conductivity, stability, activity and excellent corrosion resistance, even in high concentrations of Cl^-. However, the scarcity of noble metals poses a significant challenge for long-term availability, highlighting the need for non-precious metal-based catalysts that can be used sustainably.[7–12] NiFe-based catalysts have garnered significant attention due to their low cost and abundant availability, making them widely applicable for seawater oxidation. NiFe-based catalysts facilitate the formation of high-valence metal centers and exhibit water oxidation activity comparable to that of RuO_2.[13] In recent years, various NiFe-based electrocatalysts have been developed for the OER, including NiFe-based oxides,[14] hydroxides,[15] layered double hydroxides (LDHs)[16,17] and metal–organic frameworks (MOFs). These NiFe-based catalysts effectively reduce the overpotential in the OER process through a unique synergistic mechanism involving Ni and Fe, which significantly accelerates the kinetics of the overall electrolysis process.[18] Among the identified bimetallic LDH-based OER catalysts, NiFeLDH demonstrates the most promising performance. However, enhancing the activity of NiFeLDHs remains a challenge due to their limited active sites, poor conductivity and stability. To further improve the stability and activity of NiFeLDH-based OER catalysts, doping with

[a]*Key Laboratory of Eco-chemical Engineering, International Science and Technology Cooperation Base of Eco-chemical Engineering and Green Manufacturing, College of Environment and Safety Engineering, Qingdao University of Science and Technology, Qingdao 266042, China*

[b]*Hunan Provincial Key Laboratory of Water Treatment Functional Materials, College of Chemistry and Materials Engineering, Hunan University of Arts and Science, Changde 415000, Hunan, People's Republic of China*

[c]*College of Chemistry and Molecular Engineering, Qingdao University of Science and Technology, Qingdao 266042, PR China*

[d]*Key Laboratory of Energy Thermal Conversion and Control of Ministry of Education, School of Energy and Environment, Southeast University, Nanjing, 2111189, China. E-mail: chijingqi@qust.edu.cn; qinjunfeng@huas.edu.cn; inorchemwl@126.com*

a third metal provides a viable approach to optimizing their intrinsic activity. For NiFeLDH catalysts, the adsorption process of oxygen intermediates is significantly influenced by the electronic structure of the d-band, primarily determined by the d-orbital structure. Introducing different atomic dopants can trigger symmetry breaking in the original lattice structure, thereby rationally regulating the d-orbital configuration.[19] Moreover, research by Strasser *et al.* has shown that the OER in NiFeLDH occurs *via* the Mars van Krevelen mechanism, where Fe sites with flexible electronic structures can stabilize otherwise unstable OER intermediates at Fe or Ni sites through the formation of O-bridged Fe–Ni reaction centers and synergistic interactions with neighboring Ni sites. The limited activity and instability of conventional OER catalysts in current alkaline seawater electrolysis systems stem from their propensity to adsorb both OH^- and Cl^- ions at the majority of their active sites. This adsorption results in a concurrent OER and ClOR, impeding the selective occurrence of the OER and consequently hindering the overall seawater electrolysis process. Hence, the urgent need arises for the development of OER catalysts featuring selective active sites. By introducing heteroatoms, particularly high-valent dopants into the NiFe-LDH framework, the properties of adjacent NiFe sites can be significantly enhanced. Furthermore, the high-valent dopant can function as a Lewis acid site, locally enriching OH^- while electrostatically repelling Cl^-. This creates a surface environment that selectively adsorbs OH^- with high specificity.[20–22]

Cr is preferred due to its ease of generating high valence states and the ability of d-orbital electrons to form stable coordination structures with a variety of metals, thereby modulating the electronic structure of the material and improving material stability. In this study, Cr-doped layered double hydroxide (Cr-NiFeLDH) catalysts were prepared using a simple one-step hydrothermal method. Fig. 1a reveals that Cr doping induces a simultaneous elevation of the valence states of Ni, Fe and Cr, enhancing catalytic activity. Additionally, Cr doping stabilizes the high valence states of Ni and Fe through the introduction of oxygen vacancies and an electron transfer mechanism, which is referred to as the synergistic high-valence state stabilization effect. Furthermore, the formation of high valence states following Cr doping provides strong protection against chloride chemistry in practical applications. Benefiting

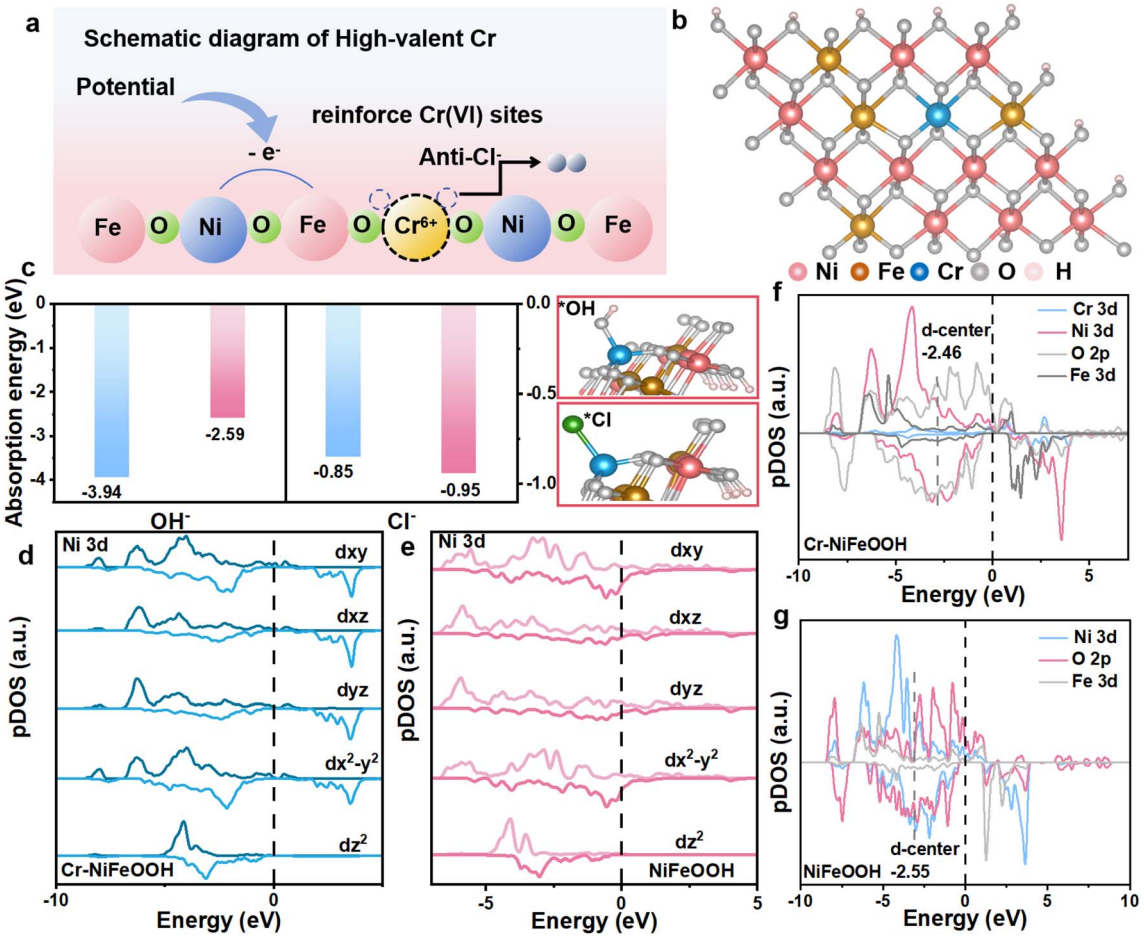

Fig. 1 (a) Design and mechanism of corrosion-resistant anodes during seawater electrolysis. Cr-NiFeLDH catalysts effectively inhibit the erosion of Cl^-. (b) Optimized structural model of Cr–NiFeOOH. (c) ΔG (*OH) and ΔG (*Cl) of Cr–NiFeOOH and NiFeOOH. Projected density of states (PDOS) of each orbital of Ni 3d in (d) Cr–NiFeOOH and (e) NiFeOOH. PDOS in the orbital coupling of (f) Cr–NiFeOOH and (g) NiFeOOH electrocatalysts.

from above, the Cr-NiFeLDH catalyst achieves continuous electrolysis in alkaline seawater at a current density of 500 mA cm^{-2} for 140 h, with low overpotentials of 300 mV and 349 mV to drive a current density of 500 and 1000 mA cm^{-2}, respectively.

Results and discussion

Theoretical studies

The most plausible γ-MOOH structure was initially used to simulate the Cr–NiFeOOH model. As illustrated in Fig. 1b, the Ni, Fe and Cr sites are readily saturated by OH species. Fig. 1c demonstrates that Cr doping significantly influences the electron transfer properties of NiFeOOH, resulting in OH^- adsorption energy of −3.94 eV for Cr–NiFeOOH, which is higher than that of NiFeOOH (−2.59 eV). This indicates that Cr–NiFeOOH exhibits a stronger affinity for OH^- adsorption compared to NiFeOOH, implying enhanced OER kinetics for Cr–NiFeOOH. In terms of Cl^- adsorption, the Cl^- adsorption energy of Cr–NiFeOOH is −0.85 eV, lower than that of NiFeOOH, suggesting a reduced affinity for Cl^- adsorption. This further highlights the superior selectivity of Cr–NiFeOOH for the OER in alkaline seawater.

In addition, the projected density of states (PDOS) of the five orbital components of nickel was calculated, as shown in Fig. 1d and e. The spin-down d_{xy}, d_{xz}, d_{yz}, $d_{x^2-y^2}$, and d_{z^2} states of Cr–NiFeOOH contribute more electron distribution around the Fermi energy level, providing additional electrons to contribute to the OER,[23,24] and the projected density of states of the five orbital components of Fe is shown in Fig. S1. The same results can be obtained as above. A comparison of the PDOS of Cr–NiFeOOH and NiFeOOH reveals that Cr doping significantly increases the density of states (DOS) at the Fermi energy level, indicating improved electron mobility and charge transfer kinetics (Fig. 1f and g). Furthermore, the d-band center (Δd) of Cr–NiFeOOH increases from −2.55 eV to −2.46 eV compared to NiFeOOH, suggesting that the d-band center of Cr–NiFeOOH is closer to the Fermi energy level compared to undoped NiFeOOH. According to d-band center theory, the interaction between adsorbates and d-electrons forms bonding and antibonding orbitals, with antibonding orbitals located below the Fermi energy level. The position of the antibonding orbitals is closely related to adsorption strength. As the antibonding center shifts toward the Fermi energy level, the energy of the antibonding state increases, resulting in stronger adsorption of OER intermediates.[25]

Preparation and characterization of Cr-NiFeLDH

Cr-NiFeLDH was successfully synthesized on nickel foam using a one-step hydrothermal method. For comparison, undoped NiFeLDH was also prepared under the same conditions. The X-ray diffraction (XRD) pattern of the synthesized NiFeLDH (Fig. S2) aligns well with the standard profile for NiFeLDH (JCPDS No. 40-0215). After Cr doping, the XRD pattern of Cr-NiFeLDH retains the same series of Bragg reflections as NiFeLDH (Fig. S3), but with slight shifts in peak positions, indicating successful incorporation of Cr. The morphology of the prepared catalyst was examined using scanning electron microscopy (SEM) and transmission electron microscopy (TEM). The above images reveal that Cr-NiFeLDH nanosheets are uniformly grown on the nickel foam and form an interconnected network structure (Fig. S4a and 2a). For comparison, the SEM image of NiFeLDH is presented in Fig. S4b, confirming that the morphology remains unchanged after Cr doping due to the presence of dense nanosheet arrays. The high-resolution transmission electron microscopy (HRTEM) image of Cr-NiFeLDH (Fig. 2b) displays lattice fringes with a spacing of 1.97 Å, corresponding to the (018) crystal facet of LDH. Energy dispersive X-ray spectroscopy (EDS) analysis of Cr-NiFeLDH demonstrates a uniform distribution of Ni, Fe and Cr throughout the catalyst (Fig. 2c). During the OER process, Cr-NiFeLDH undergoes a phase transition, resulting in its transformation into a phase that is highly favorable for catalysis. To ascertain the stability of the catalyst after reaction, we conducted comprehensive testing of the corresponding EDS elemental images of the Cr-NiFeLDH-R. The results, as depicted in Fig. S5, show a uniform distribution of the three constituent elements. To quantify the specific amount of Cr in Cr-NiFeLDH, inductively coupled plasma optical emission spectroscopy (ICP-OES) measurements were conducted (Table S1), confirming successful incorporation of Cr. As shown in Fig. 2d, the peak at $g = 2.004$ indicates the presence of nonmetallic vacancies in the catalyst. The higher intensity of this peak in Cr-NiFeLDH compared to NiFeLDH suggests a significant increase in oxygen vacancies, likely attributed to Cr loss during the phase transition. Differential charge calculations indicate that the introduction of oxygen vacancies greatly enhances electron migration around Ni, Fe and Cr (Fig. 2e). X-ray absorption near-edge structure (XANES) analysis reveals that the XANES spectrum of Cr-NiFeLDH is positively shifted relative to those of NiO, Ni_2O_3, and NiOOH (Fig. 2f), suggesting that the average valence state of Ni in Cr-NiFeLDH is slightly above +3. The Fourier-transform extended X-ray absorption fine structure (FT-EXAFS) spectrum of Cr-NiFeLDH (Fig. 2g) closely resembles the characteristic peak of NiOOH, demonstrating the formation of an active NiOOH phase during the phase transition in the oxygen evolution reaction (OER) process. Wavelet transform (WT) analysis of the EXAFS data indicates that Cr-NiFeLDH has a coordination environment similar to that of NiOOH (Fig. 2h), which is consistent with the EXAFS results.

X-ray photoelectron spectroscopy (XPS) analysis of Cr-NiFeLDH and NiFeLDH reveals significant surface chemical changes after the introduction of Cr (Fig. S6). The binding energy peaks for Ni 2p and Fe 2p shift to higher values, indicating an increase in the valence states of both Ni and Fe in Cr-NiFeLDH. Additionally, the structural transformation of Cr-NiFeLDH and NiFeLDH before and after the OER performance test was examined using XPS. The high-resolution Ni 2p XPS spectra for Cr-NiFeLDH and Cr-NiFeLDH after the OER test (denoted as Cr-NiFeLDH-R) are shown in Fig. S7. The peaks for Cr-NiFeLDH centered at 856 eV and 874 eV correspond to Ni $2p_{3/2}$ and Ni $2p_{1/2}$, respectively, which are attributed to the Ni^{2+}

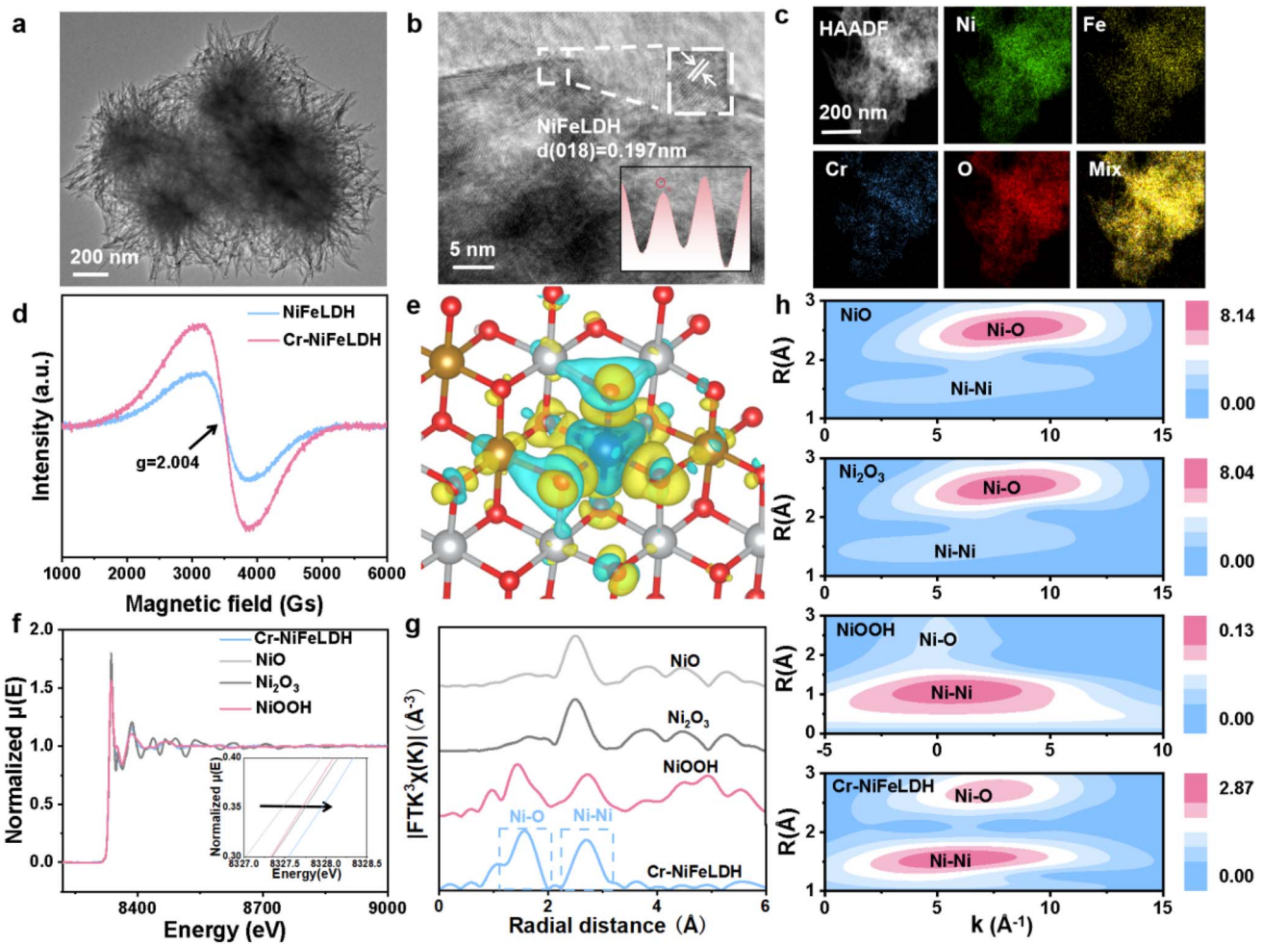

Fig. 2 (a) TEM and (b) HRTEM image of Cr-NiFeLDH. (c) Corresponding elemental distributions of Cr-NiFeLDH. (d) EPR spectra of Cr-NiFeLDH and NiFeLDH. (e) Charge density difference of Cr-NiFeLDH. (f) Ni K-edge XANES and (g) EXAFS of NiO, Ni_2O_3, NiOOH, and Cr-NiFeLDH. (h) The wavelet transform plots of different samples.

state in Cr-NiFeLDH.[26] The peaks at 862.5 eV and 880.5 eV are associated with Ni^{3+} $2p_{3/2}$ and Ni^{3+} $2p_{1/2}$ states, likely arising from unavoidable surface oxidation when exposed to air.[27] After the OER test, the intensity of the Ni^{2+} peak significantly decreases, while the intensity of the Ni^{3+} peak increases markedly, indicating that the surface of Cr-NiFeLDH may have undergone reconstruction during the OER process, with Ni^{2+} being oxidized to form NiOOH. Moreover, Fig. S8 illustrates the Fe 2p spin states of Cr-NiFeLDH, showing an increase in the valence state of Fe. Similarly, Fig. S9 presents the spin states of Cr 2p, where the peak intensity corresponding to Cr^{6+} has also increased, further confirming that the valence state of Cr has risen as well. Fig. S10 and S11 shows the Ni and Fe 2p spin states of NiFeLDH, respectively. The binding energies are basically unshifted, and there is no significant change in the peak intensities of Ni and Fe, indicating that the valence states of Ni and Fe basically remain unchanged in the absence of Cr doping, which suggests that doping with high-valent Cr is the cause of the change in the valence states of Ni and Fe. In addition, the O 1 s spin state is shown in Fig. S12.

Evaluation of OER activity and application of anodes in AEM electrolyzers

The performance of the prepared catalyst was evaluated in a standard three-electrode system. Initially, the performance of Cr-NiFeLDH in 1.0 M KOH solution was tested (Fig. S13), and the overpotential was only 230 mV at 1000 mA cm^{-2}. Subsequently, electrochemical tests were conducted for Cr-NiFeLDH, NiFeLDH, and RuO_2 in a solution of 1.0 M KOH + seawater (SW) to examine the impact of Cr doping on catalyst performance. As illustrated in Fig. 3a, Cr-NiFeLDH exhibits excellent alkaline OER performance. At a current density of 1000 mA cm^{-2}, it demonstrates an ultra-low overpotential of only 349 mV, outperforming commercial RuO_2/NF. At the same current density, the overpotential for Cr-NiFeLDH is lower than that for NiFeLDH, indicating that Cr doping enhances the alkaline OER activity of Cr-NiFeLDH. The reaction kinetics and intrinsic activity of the catalyst in seawater were further investigated using Tafel slope analysis, electrochemical impedance spectroscopy (EIS), and turnover frequency (TOF) tests (Fig. S14). As shown in Fig. 3b, Cr-NiFeLDH exhibits the smallest Tafel slope

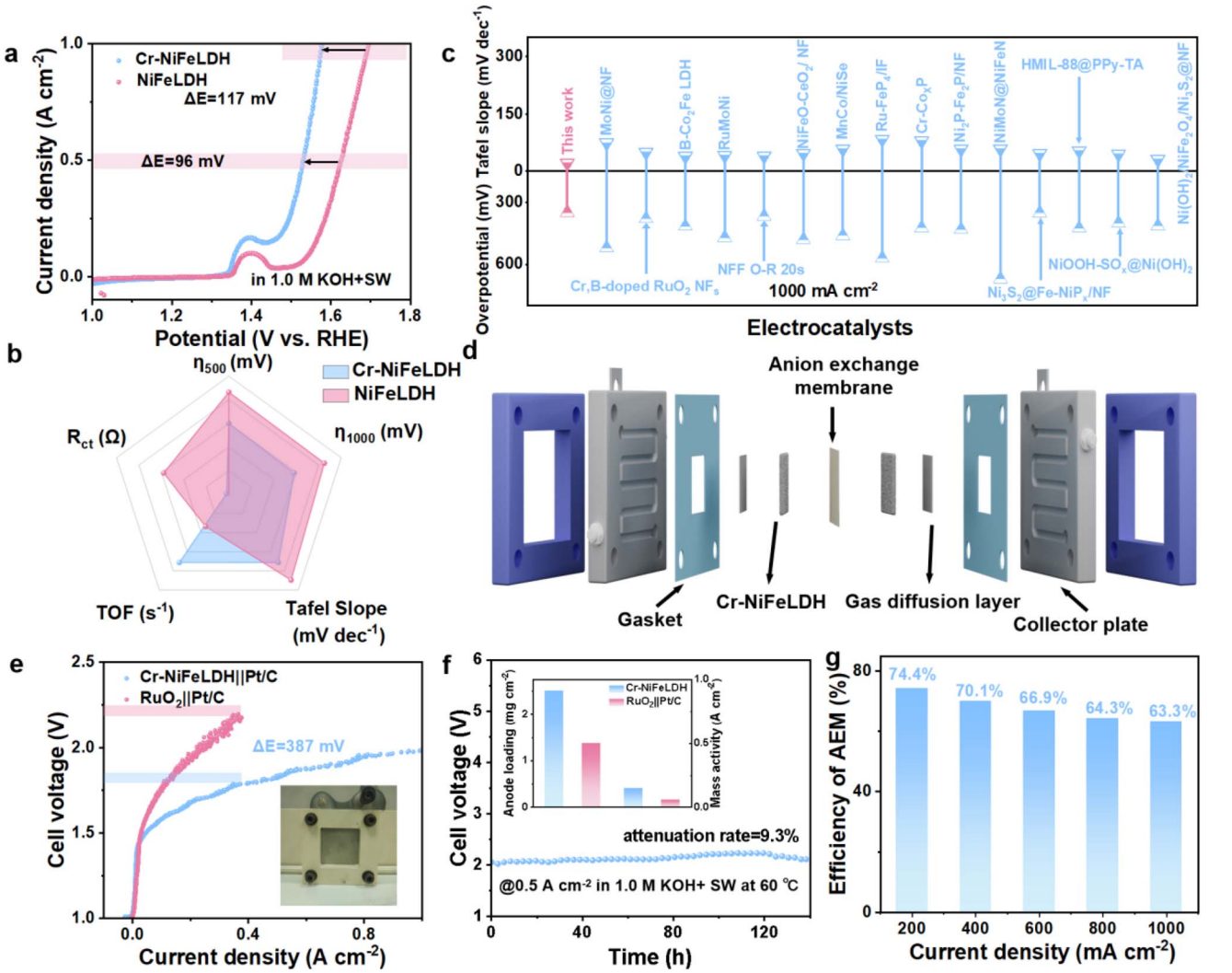

Fig. 3 (a) LSV curves in 1.0 M KOH+SW. (b) Radar images of various performance indicators of Cr-NiFeLDH and NiFeLDH. (c) Comparison of catalytic performance between Cr-NiFeLDH and other reported OER catalysts reported. (d) Diagram of the AEM electrolyzer. (e) LSV of Cr-NiFeLDH||Pt/C and RuO_2||Pt/C. (f) Stability of the AEM electrolyzer operating at 500 mA cm^{-2}. (g) Efficiency of the AEM electrolyzer.

and the lowest electrochemical impedance, confirming its excellent reaction kinetics and demonstrating rapid charge transfer between the electrolyte and the electrode. Additionally, Cr-NiFeLDH has the highest turnover frequency (TOF), suggesting that the catalyst offers a greater number of active sites and possesses superior intrinsic activity compared to other nickel-based catalysts reported in recent years (Fig. 3c and Table S2). Long-term stability is also a critical parameter for evaluating the OER activity of electrocatalysts, particularly at industrial current densities. As depicted in Fig. S15, Cr-NiFeLDH is stably electrolyzed for over 40 h in 1.0 M KOH + SW solution at a current density of 100 mA cm^{-2} without significant voltage loss. Furthermore, an alkaline seawater anion exchange membrane (AEM) electrolytic cell was assembled with Cr-NiFeLDH as the anode. A low cell voltage of only 1.98 V is required to drive a current density of 2000 mA cm^{-2}, while maintaining stable electrocatalytic activity for over 140 h at 500 mA cm^{-2} (Fig. 3d–f). Additionally, we calculated the electrolysis efficiency of the Cr-NiFeLDH||Pt/C system, which is found to be 68.8% at a current density of 500 mA cm^{-2} (Fig. 3g).[28,29] Table S3 shows the comparison of reported electrolyzer efficiencies with the present work. These results demonstrate that the Cr-doped NiFeLDH catalyst possesses excellent OER stability and activity in alkaline seawater. The observed performance improvements highlight the potential for industrial alkaline seawater electrolysis using AEM electrolyzers.

To further elucidate the detailed mechanism of the OER on the surface of Cr-NiFeLDH, we investigated the surface evolution of Cr-NiFeLDH in an alkaline electrolyte at different voltages using *in situ* impedance spectroscopy, *in situ* Raman spectroscopy and quasi *in situ* XPS. The electron transfer during the OER process was analyzed using the Bode diagram (Fig. 4a). When the OER potential of Cr-NiFeLDH exceeds 1.33 V, the phase angle in the high-frequency region diminishes, indicating the conversion of $Ni(OH)_2$ to NiOOH at this voltage. Simultaneously, a decrease in the phase angle in the low-

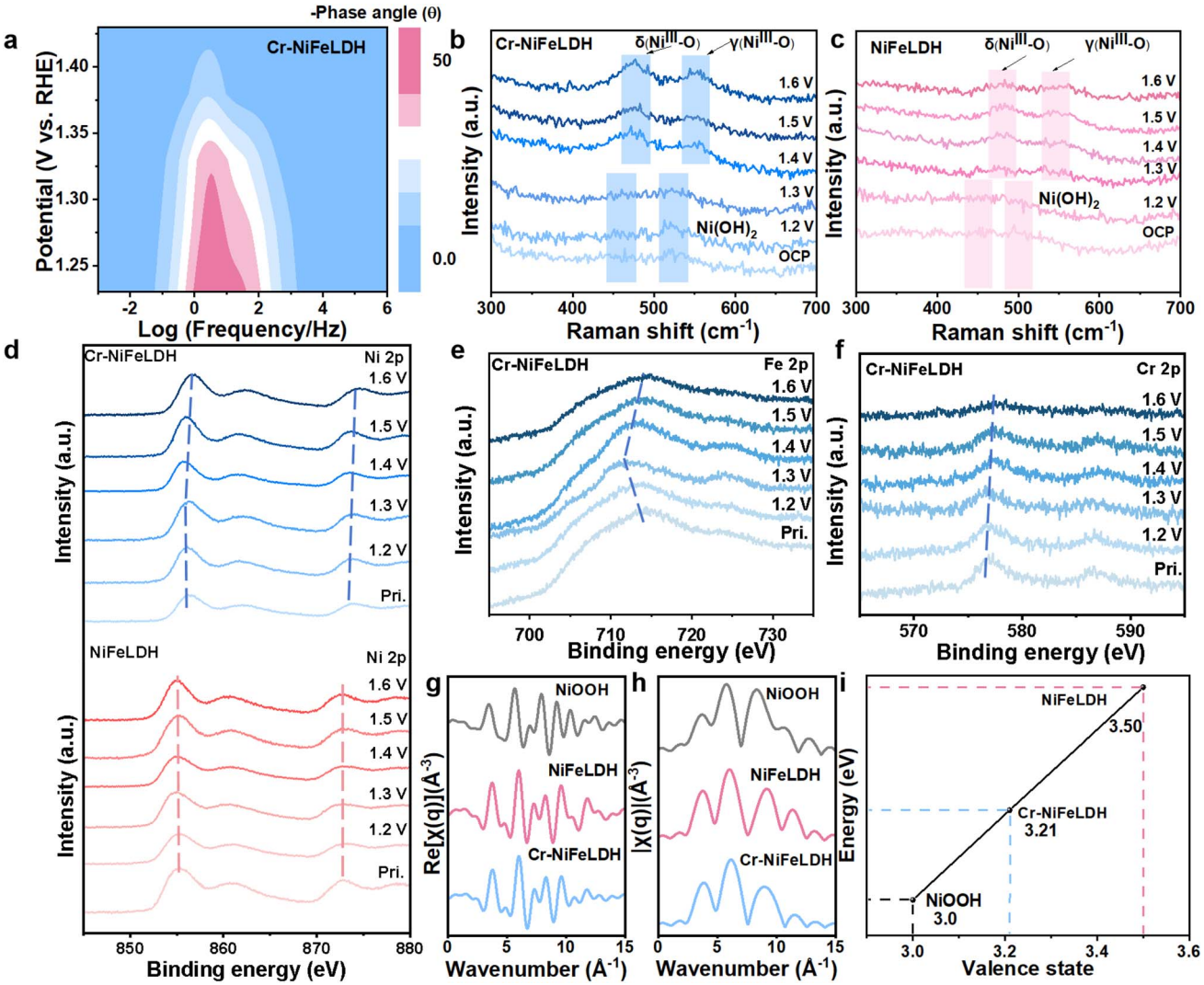

Fig. 4 (a) *In situ* Bode diagram of Cr-NiFeLDH. (b) *In situ* Raman spectra of Cr-NiFeLDH and (c) NiFeLDH. (d) Ni 2p, (e) Fe 2p, and (f) Cr 2p. XPS spectra of Cr-NiFeLDH at different voltages. (g-h) Plots in *q* space of NiOOH, NiFeLDH and Cr-NiFeLDH. (i) XANES valence state fitting line graph.

frequency region is observed when the potential exceeds 1.33 V, signifying a significant increase in the electron transport rate and a similar trend is noted for NiFeLDH (Fig. S16), where NiFeLDH exhibits a higher phase angle at the OER potential, suggesting that the electron transfer barrier for NiFeLDH is greater than that for Cr-NiFeLDH. The Nyquist plot (Fig. S17) further supports this finding, as the substantial reduction in the semicircle at 1.38 V confirms rapid electron transfer in Cr-NiFeLDH. In a 1.0 M KOH + seawater solution, we detect the generation of active species during the electrolysis of the catalyst within the potential range of 1.2 V to 1.6 V. As shown in Fig. 4b, two Raman bands at 400-600 cm^{-1} appear simultaneously at 451 and 532 cm^{-1} before 1.3 V, corresponding to the Ni(OH)$_2$ phase. As the voltage increases to 1.3 V, two strong Raman bands at 460 cm^{-1} and 541 cm^{-1} can be indexed to NiOOH and the intensity of the NiOOH peak progressively increases with the voltage, demonstrating that Cr-NiFeLDH begins to undergo a phase transition to form the catalytically favorable NiOOH phase at 1.3 V. For comparison, the *in situ* Raman spectra of NiFeLDH are presented in Fig. 4c. Notably, before reaching 1.4 V, there are no significant changes in the Raman spectrum of NiFeLDH. At 1.4 V, the corresponding peaks for NiOOH emerge around 478 cm^{-1} and 544 cm^{-1}. Compared to Cr-NiFeLDH, these peaks are weaker and more distinct in the contour map, indicating that Cr doping promotes the formation of the catalytic NiOOH phase. To assess the influence of Cr doping on the valence states of Ni and Fe, we analyzed the XPS spectra of Cr-NiFeLDH at varying voltages. The Ni 2p spectrum depicted in Fig. 4d displays a characteristic peak around 856.2 eV, corresponding to the spin–orbit splitting of Ni 2p$_{3/2}$. As the voltage increases, the Ni 2p$_{3/2}$ peak exhibits a positive shift, indicating a continuous increase in the valence state of Ni within the catalyst. When the voltage reaches 1.6 V, the main peak of Ni shifts forward by 0.6 eV compared to the state without applied voltage, which shift positively than that of NiFeLDH. This finding suggests that the oxidation state of the

catalyst is more pronounced after Cr doping. As shown in Fig. 4e, the Fe 2p spectrum reveals a characteristic peak around 715 eV, corresponding to the Fe $2p_{3/2}$ spin–orbit splitting. When the voltage increases from open circuit potential (OCP) to 1.3 V, the Fe $2p_{3/2}$ peak shifts negatively from 714 to 712 eV, indicating an accumulation of electrons at the Fe site during the OER phase transition. Cr preferentially replaces Ni, and Cr^{3+} transfers electrons to Fe^{3+} *via* an oxygen bridge, resulting in a temporary decrease in Fe valence. As the voltage rises to 1.6 V, the Fe $2p_{3/2}$ peak moves from 712 to 714.1 eV, suggesting a reversal in the direction of electron transfer at the Fe site. This may be due to the fact that during the OER process, some Cr loses electrons to form high-valent Cr (Cr^{6+}), and its high electronegativity attracts the surrounding electrons, leading to a decrease in the local electron density at the Fe site. This electron transfer may elevate the oxidation state of Fe. The O 2p spectrum of Cr-NiFeLDH is presented in Fig. S18, where the characteristic peak position shifts toward lower binding energy, indicating that electrons are transferred from metallic sites to O, resulting in an accumulation of electrons around O. The Cr 2p spectrum shown in Fig. 4f also exhibits a positive shift in the Cr $2p_{3/2}$ peak with increasing voltage, indicating that the valence state of Cr increases gradually, further confirming the generation of higher valence Cr during the activation process. The plots in *q*-space depicted in Fig. 4g and h indicate that the spectral features of Cr-NiFeLDH, NiFeLDH and NiOOH are relatively similar, confirming that the valence state of Ni increases after the activation of both catalysts. Further calculations reveal that the average valence states of Ni in Cr-NiFeLDH and NiFeLDH are approximately 3.21 and 3.50, respectively (Fig. 4i). The XANES spectrum of NiFeLDH presented in Fig. S19 again illustrates the decrease in the valence state of Ni after Cr doping. Collectively, these *in situ* characterization results indicate that Cr doping effectively modulates the electron distribution of Ni and mitigates the over-oxidation of the Ni^{3+} active site. This modification enhances the long-term

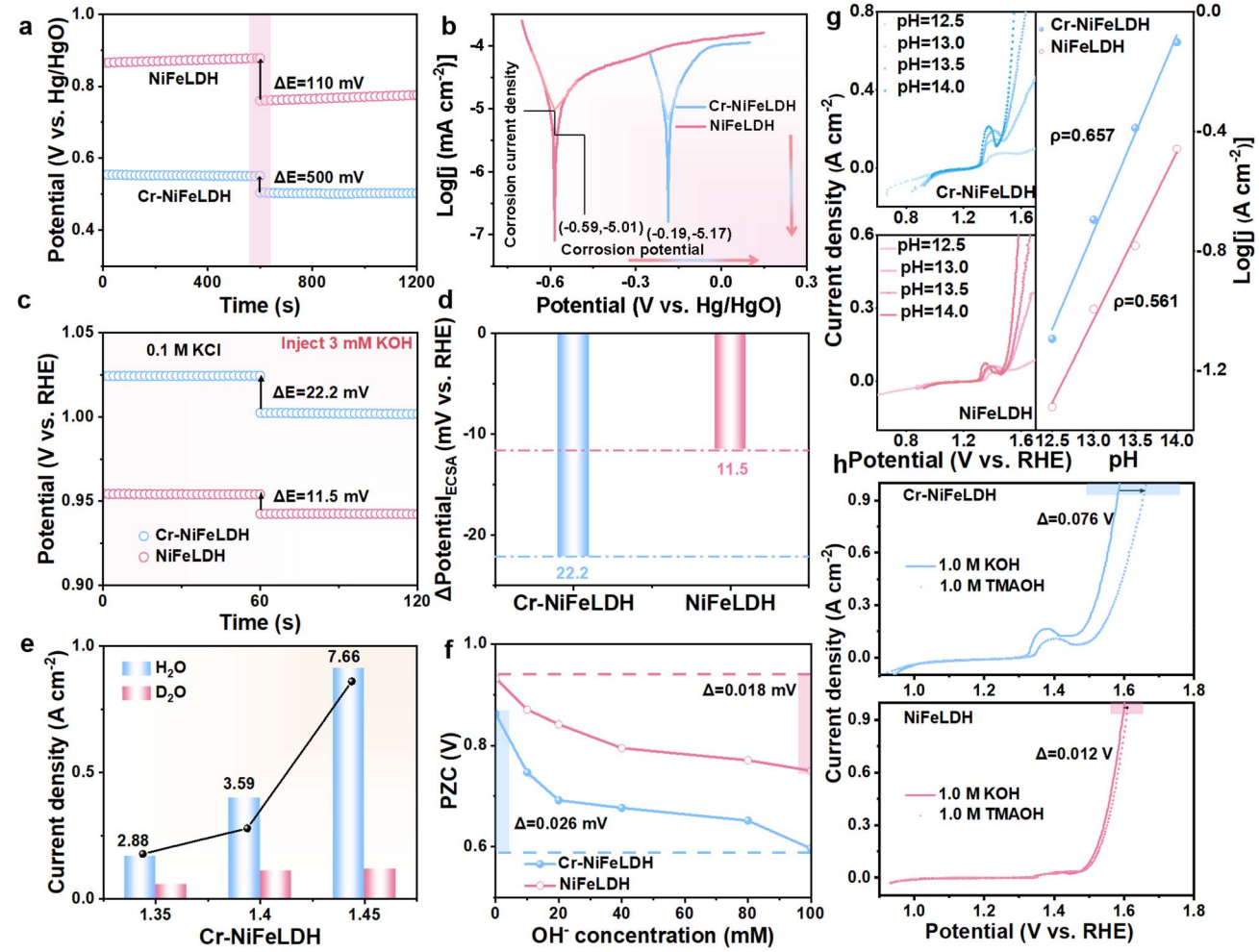

Fig. 5 (a) Chronopotentiometry response at 10 mA cm^{-2}. The initial test was carried out in 1.0 M NaOH for 600 s and 0.5 mM EDTA-2Na was added after 600 s. (b) Tafel plots of Cr-NiFeLDH and NiFeLDH. (c) Open circuit potential measured in 0.1 M KCl solution before and after the injection of 3 mM KOH over Cr-NiFeLDH and NiFeLDH. (d) Change in potential of Cr-NiFeLDH and NiFeLDH after normalization by the total ECSA. (e) KIE values of Cr-NiFeLDH and NiFeLDH. (f) Zero charge potential (PZC) of Cr-NiFeLDH and NiFeLDH. (g) Polarization curves with ρ_{RHE} values. (h) LSV curves in alkaline seawater with/without TMA^+ with 100% *iR* correction.

stability and OER catalytic activity of Cr-NiFeLDH in alkaline seawater.

The issue of poor stability and low activity of OER catalysts in seawater electrolysis is largely due to the fact that most OER active sites are also reactive towards the ClOR. We investigated their corrosion resistance and selective adsorption capacity through electrochemical tests and computational modeling. Disodium ethylenediaminetetraacetic acid (EDTA-2Na) was added to the electrolyte to examine the repulsion of weakly nucleophilic negatively charged substances (*e.g.*, Cl^- and $EDTA^{2-}$) by various ionic layers. As illustrated in Fig. 5a, the addition of 5.0 mM EDTA-2Na to 1.0 M NaOH results in a decrease in potential at 10 mA cm^{-2} across multiple electrodes. This indicates that $EDTA^{2-}$ can undergo a nucleophilic reaction with the electrode, leading to its further oxidation.[30] The smaller the change in potential (ΔE), the weaker the nucleophilicity of the electrode, and the greater the repulsion of $EDTA^{2-}$ and Cl^-. Notably, NiFeLDH shows the highest voltage change ($\Delta E = 110$ mV), while Cr-NiFeLDH demonstrates a lower ΔE (50 mV) and stronger repulsion by the ionic layer. In Fig. 5b, we assessed the corrosion resistance of Cr-NiFeLDH and NiFeLDH using corrosion polarization curves.[31] The J_{corr} and E_{corr} values for Cr-NiFeLDH are -5.01 mA cm^{-2} and -0.59 V, respectively, outperforming that of NiFeLDH and indicating enhanced corrosion resistance to seawater due to Cr doping. The open-circuit potentials (OCP) were measured in 0.1 M KCl solution before and after the addition of 3.0 mM KOH for Cr-NiFeLDH and NiFeLDH, as shown in Fig. 5c. Fig. 5d illustrates the changes in potentials for Cr-NiFeLDH and NiFeLDH after normalization by the electrochemical surface area (ECSA). The larger negative shift in the ECSA-normalized OCP for Cr-NiFeLDH compared to NiFeLDH after the addition of 3.0 mM KOH indicates stronger OH^- adsorption on the surface of Cr-NiFeLDH.[32] Deuterium kinetic isotope effect (KIE) experiments were conducted to evaluate the catalytic response to OH^-. As depicted in Fig. 5e, S20 and S21, the KIE values for Cr-NiFeLDH are consistently smaller than those for NiFeLDH at all voltages, suggesting that Cr-NiFeLDH has a stronger binding capacity for OH^- during the OER process.[33] Fig. 5f shows that the point of zero charge (PZC) for Cr-NiFeLDH and NiFeLDH shifts negatively with increasing OH^- concentration, indicating specific OH^- adsorption on the catalyst surface per the Esin-Markov effect. The more pronounced negative shift in the PZC for Cr-NiFeLDH compared to NiFeLDH after OH^- addition suggests enhanced OH^- adsorption on the inner Helmholtz plane. We further examined the origin of OER activity, noting its pH dependence for all catalysts. As shown in Fig. 5g, both Cr-NiFeLDH and NiFeLDH are significantly impacted when the pH increases from 12.5 to 14, which indicates the lattice oxygen mechanism (LOM) pathway. The proton reactivity level (ρ_{RHE}) for Cr-NiFeLDH and NiFeLDH is 0.6572 and 0.5603, respectively, indicating that Cr incorporation promotes lattice oxygen involvement in the OER process.[34,35] Additionally, we used the tetramethylammonium cation (TMA^+) as a chemical probe to confirm the surface reaction pathway followed by the LOM step. Replacing K^+ with TMA^+ in alkaline solution leads to a more significant activity change for Cr-NiFeLDH compared to NiFeLDH (Fig. 5h); after TMA^+ is introduced into the electrolyte, it can specifically interact with negatively charged surface oxygenates. The OER activity of Cr-NiFeLDH was significantly reduced when 1.0 M TMAOH was used as the electrolyte compared to 1.0 M KOH, suggesting that the strong binding of TMA^+ inhibits the OER through LOM, whereas the OER properties of NiFeLDH were not significantly changed under 1.0 M KOH and 1.0 M TMAOH conditions. These results indicate the presence of LOM in the OER of Cr-NiFeLDH, and also this explains the high OER activity of Cr-NiFeLDH.[36,37]

Conclusion

In conclusion, we have successfully synthesized NiFe-LDH doped with high valence Cr metal (Cr-NiFeLDH), demonstrating its efficacy as an OER catalyst for seawater electrolysis. The enhanced performance of Cr-NiFeLDH is likely due to the synergistic stabilization provided by the Cr dopant in conjunction with the bimetallic NiFe sites, which collectively alter the electronic structure of the entire system. Furthermore, high-valent Cr possesses the capability to repel Cl^- and reduces its competition with the OER, thus further improving the selectivity of seawater electrolysis. Notably, the overpotentials required to achieve current densities of 500 and 1000 mA cm^{-2} are remarkably low at only 300 and 349 mV, respectively, indicating high catalytic activity. Furthermore, the Cr-NiFeLDH is employed in an industrial anion exchange membrane (AEM) electrolyzer, demonstrating sustainable long-term electrolysis for up to 140 h. This study provides new insights into the synergistic effects of multimetallic oxygen evolution catalysts, potentially paving the way for advancements in seawater electrolysis.

Author contributions

Chenxi Liu: investigation, data curation, conceptualization, formal analysis, validation, writing-original draft. Zefeng Teng: conceptualization, writing-review & editing, supervision, funding acquisition. Xu Liu: formal analysis, data curation, conceptualization, validation. Rui Zhang: data curation, conceptualization, validation. Jingqi Chi, Jiawei Zhu: supervision, validation, conceptualization. Junfeng Qin: supervision, validation. Xiaobin Liu, Zexing Wu: supervision, validation, funding acquisition. Lei Wang: writing-review & editing, funding acquisition, supervision.

Conflicts of interest

The authors declare that they have no known competing financial interests or personal relationships that could have appeared to influence the work reported in this paper.

Data availability

The datasets generated during and/or analysed during the current study are not publicly available due to restrictions

applied to the availability of these data but are available from the authors on reasonable request.

Supplementary information is available and includes experimental procedures, char-acterization data of the materials (XRD, XPS, SEM, TEM, ICP-OES, PDOS, XAS) and computational details. See DOI: https://doi.org/10.1039/d5sc02818c.

Acknowledgements

This work was financially supported by the National Natural Science Foundation of China (52072197, 52174283, and 22301156), the Natural Science Foundation of Shandong Province (ZR2024QB012), the Qingdao Natural Science Foundation (24-4-4-zrjj-16-jch), and Shandong Province "Double-Hundred Talent Plan" (WST2020003).

References

1 M. Chatenet, B. G. Pollet, D. R. Dekel, F. Dionigi, J. Deseure, P. Millet, R. D. Braatz, M. Z. Bazant, M. Eikerling and I. Staffell, Water electrolysis: from textbook knowledge to the latest scientific strategies and industrial developments, *Chem. Soc. Rev.*, 2022, **51**, 4583.

2 X. Wang, S. Xi, P. Huang, Y. Du, H. Zhong, Q. Wang, A. Borgna, Y.-W. Zhang, Z. Wang, H. Wang, Z. G. Yu, W. S. V. Lee and J. Xue, Pivotal role of reversible NiO_6 geometric conversion in oxygen evolution, *Nature*, 2022, **611**, 702–708.

3 P. Zhang, C. Zhang, L. Wang, J. Dong, D. Gai, W. Wang, T. S. Nguyen, C. T. Yavuz, X. Zou and G. Zhu, Basic Alkylamine Functionalized PAF-1 Hybrid Membrane with High Compatibility for Superior CO_2 Separation from Flue Gas, *Adv. Funct. Mater.*, 2022, **33**, 2210091.

4 H. Liu, W. Shen, H. Jin, J. Xu, P. Xi, J. Dong, Y. Zheng and S. Z. Qiao, High-Performance Alkaline Seawater Electrolysis with Anomalous Chloride Promoted Oxygen Evolution Reaction, *Angew. Chem., Int. Ed.*, 2023, **62**, e202311674.

5 Y. Kuang, M. J. Kenney, Y. Meng, W. H. Hung, Y. Liu, J. E. Huang, R. Prasanna, P. Li, Y. Li, L. Wang, M. C. Lin, M. D. McGehee, X. Sun and H. Dai, Solar-driven, highly sustained splitting of seawater into hydrogen and oxygen fuels, *Proc. Natl. Acad. Sci. U. S. A.*, 2019, **116**, 6624–6629.

6 L. Yang, H. Liu, Y. Li, L. Zhong, Z. Jin, X. Xu, D. Cao and Z. Chen, Customizing Bonding Affinity with Multi-Intermediates via Interfacial Electron Capture to Boost Hydrogen Evolution in Alkaline Water Electrolysis, *Angew. Chem., Int. Ed.*, 2024, **64**, e202500287.

7 Z. Li, Y. Yao, S. Sun, J. Liang, S. Hong, H. Zhang, C. Yang, X. Zhang, Z. Cai, J. Li, Y. Ren, Y. Luo, D. Zheng, X. He, Q. Liu, Y. Wang, F. Gong, X. Sun and B. Tang, Carbon Oxyanion Self-Transformation on NiFe Oxalates Enables Long-Term Ampere-Level Current Density Seawater Oxidation, *Angew. Chem., Int. Ed.*, 2024, **63**, e202316522.

8 L. Yu, J. Xiao, C. Huang, J. Zhou, M. Qiu, Y. Yu, Z. Ren, C. W. Chu and J. C. Yu, High-performance seawater oxidation by a homogeneous multimetallic layered double hydroxide electrocatalyst, *Proc. Natl. Acad. Sci. U. S. A.*, 2022, **119**, 6624.

9 L. Zhang, L. Li, J. Liang, X. Fan, X. He, J. Chen, J. Li, Z. Li, Z. Cai, S. Sun, D. Zheng, Y. Luo, H. Yan, Q. Liu, A. A. Alshehri, X. Guo, X. Sun and B. Ying, Highly efficient and stable oxygen evolution from seawater enabled by a hierarchical $NiMoS_x$ microcolumn@NiFe-layered double hydroxide nanosheet array, *Inorg. Chem. Front.*, 2023, **10**, 2766–2775.

10 E. Enkhtuvshin, S. Yeo, H. Choi, K. M. Kim, B. S. An, S. Biswas, Y. Lee, A. K. Nayak, J. U. Jang, K. H. Na, W. Y. Choi, G. Ali, K. H. Chae, M. Akbar, K. Y. Chung, K. Yoo, Y. C. Chung, T. H. Shin, H. Kim, C. Y. Chung and H. Han, Surface Reconstruction of Ni–Fe Layered Double Hydroxide Inducing Chloride Ion Blocking Materials for Outstanding Overall Seawater Splitting, *Adv. Funct. Mater.*, 2023, **33**, 2214069.

11 Y. Yao, S. Sun, H. Zhang, Z. Li, C. Yang, Z. Cai, X. He, K. Dong, Y. Luo, Y. Wang, Y. Ren, Q. Liu, D. Zheng, W. Zhuang, B. Tang, X. Sun and W. W. Hu, Enhancing the stability of NiFe-layered double hydroxide nanosheet array for alkaline seawater oxidation by Ce doping, *J. Energy Chem.*, 2024, **91**, 306–312.

12 X. Dong, H. Yan, Y. Jiao, D. Guo, A. Wu, G. Yang, X. Shi, C. Tian and H. Fu, 3D hierarchical V–Ni-based nitride heterostructure as a highly efficient pH-universal electrocatalyst for the hydrogen evolution reaction, *J. Mater. Chem. A*, 2019, **7**, 15823–15830.

13 H. Cai, J. Liang, Z. Li, T. Yan, C. Yang, H. Sun, M. Yue, X. Liu, T. Xie, Y. Wang, T. Li, Y. Luo, D. Zheng, Q. Liu, J. Zhao, X. Sun and B. Tang, Stabilizing NiFe sites by high-dispersity of nanosized and anionic Cr species toward durable seawater oxidation, *Nat. Commun.*, 2024, **15**, 6624.

14 X. Yuan, Y. Wang, Z. Xu, T. Zhou and L. Fang, Training large-scale optoelectronic neural networks with dual-neuron optical-artificial learning, *Nat. Commun.*, 2023, **14**, 7110.

15 Z. Lei, J. Bai, Y. Li, Z. Wang and C. Zhao, Fabrication of Nanoporous Nickel–Iron Hydroxylphosphate Composite as Bifunctional and Reversible Catalyst for Highly Efficient Intermittent Water Splitting, *ACS Appl. Mater. Interfaces*, 2017, **9**, 35837–35846.

16 Z. Cai, D. Zhou, M. Wang, S. M. Bak, Y. Wu, Z. Wu, Y. Tian, X. Xiong, Y. Li, W. Liu, S. Siahrostami, Y. Kuang, X. Q. Yang, H. Duan, Z. Feng, H. Wang and X. Sun, Introducing Fe^{2+} into Nickel-Iron Layered Double Hydroxide: Local Structure Modulated Water Oxidation Activity, *Angew. Chem., Int. Ed.*, 2018, **57**, 9392–9396.

17 S. Zhao, Y. Tang, X. Yu and J. Li, Superior reactivity of heterogeneous single-cluster catalysts for semi-hydrogenation of acetylene, *Sci. China Mater.*, 2023, **66**, 3912–3921.

18 J. Liu, Y. Liu, X. Mu, H. Jang, Z. Lei, S. Jiao, P. Yan, M. G. Kim and R. Cao, Boosting Activity and Stability of Electrodeposited Amorphous Ce-Doped NiFe-Based Catalyst for Electrochemical Water Oxidation, *Adv. Funct. Mater.*, 2022, **32**, 2204086.

19 X. Wang, W. Pi, S. Hu, H. Bao, N. Yao and W. Luo, Boosting Oxygen Evolution Reaction Performance on NiFe-Based Catalysts Through d-Orbital Hybridization, *Nano-Micro Lett.*, 2024, **17**, 11.
20 F. Dionigi, J. Zhu, Z. H. Zeng, T. Merzdorf, H. Sarodnik, M. Gliech, L. J. Pan, W. X. Li, J. Greeley and P. Strasser, Intrinsic Electrocatalytic Activity for Oxygen Evolution of Crystalline 3d-Transition Metal Layered Double Hydroxides, *Angew. Chem., Int. Ed.*, 2021, **60**, 14446–14457.
21 M. H. Wang, Z. X. Lou, X. Wu, Y. Liu, J. Y. Zhao, K. Z. Sun, W. X. Li, J. Chen, H. Y. Yuan, M. Zhu, S. Dai, P. F. Liu and H. G. Yang, Operando High-Valence Cr-Modified NiFe Hydroxides for Water Oxidation, *Small*, 2022, **18**, 2200303.
22 R. Tong, Z. Sun, F. Zhang, X. Wang, J. Xu, X. Shi, S. Wang and H. Pan, N and V Coincorporated Ni Nanosheets for Enhanced Hydrogen Evolution Reaction, *ACS Sustain. Chem. Eng.*, 2018, **6**, 16525–16531.
23 M. T. Greiner, T. E. Jones, S. Beeg, L. Zwiener, M. Scherzer, F. Girgsdies, S. Piccinin, M. Armbrüster, A. Knop-Gericke and R. Schlögl, Free-atom-like d states in single-atom alloy catalysts, *Nat. Chem.*, 2018, **10**, 1008–1015.
24 J. Zhu, T. Cui, J. Chi, T. Wang, L. Guo, X. Liu, Z. Wu, J. Lai and L. Wang, Frustrated Lewis Pair Mediated f-p-d Orbital Coupling: Achieving Selective Seawater Oxidation and Breaking *OH and *OOH Scaling Relationship, *Angew. Chem., Int. Ed.*, 2024, **64**, e202414721.
25 D. Y. Kuo, H. Paik, J. Kloppenburg, B. Faeth, K. M. Shen, D. G. Schlom, G. Hautier and J. Suntivich, Measurements of Oxygen Electroadsorption Energies and Oxygen Evolution Reaction on RuO_2(110): A Discussion of the Sabatier Principle and Its Role in Electrocatalysis, *J. Am. Chem. Soc.*, 2018, **140**, 17597–17605.
26 J. Jiang, F. Sun, S. Zhou, W. Hu, H. Zhang, J. Dong, Z. Jiang, J. Zhao, J. Li, W. Yan and M. Wang, Atomic-level insight into super-efficient electrocatalytic oxygen evolution on iron and vanadium co-doped nickel (oxy)hydroxide, *Nat. Commun.*, 2018, **9**, 2885.
27 W. Zhang, Y. Wu, J. Qi, M. Chen and R. Cao, A Thin NiFe Hydroxide Film Formed by Stepwise Electrodeposition Strategy with Significantly Improved Catalytic Water Oxidation Efficiency, *Adv. Energy Mater.*, 2017, **7**, 1602547.
28 S. Hao, H. Sheng, M. Liu, J. Huang, G. Zheng, F. Zhang, X. Liu, Z. Su, J. Hu, Y. Qian, L. Zhou, Y. He, B. Song, L. Lei, X. Zhang and S. Jin, Torsion strained iridium oxide for efficient acidic water oxidation in proton exchange membrane electrolyzers, *Nat. Nanotechnol.*, 2021, **16**, 1371–1377.
29 J. Chang, G. Wang, Z. Yang, B. Li, Q. Wang, R. Kuliiev, N. Orlovskaya, M. Gu, Y. Du, G. Wang and Y. Yang, Dual-Doping and Synergism toward High-Performance Seawater Electrolysis, *Adv. Mater.*, 2021, **33**, 2101425.
30 W. Liu, J. Yu, M. G. Sendeku, T. Li, W. Gao, G. Yang, Y. Kuang and X. Sun, Ferricyanide Armed Anodes Enable Stable Water Oxidation in Saturated Saline Water at 2 A/cm^2, *Angew. Chem., Int. Ed.*, 2023, **62**, e202309882.
31 L. Zhou, C. Yang, W. Zhu, R. Li, X. Pang, Y. Zhen, C. Wang, L. Gao, F. Fu, Z. Gao and Y. Liang, Boosting Alkaline Hydrogen Evolution Reaction via an Unexpected Dynamic Evolution of Molybdenum and Selenium on $MoSe_2$ Electrode, *Adv. Energy Mater.*, 2022, **12**, 2202367.
32 B. Huang, J. Yan, Z. Li, L. Chen and J. Shi, Anode-Electrolyte Interfacial Acidity Regulation Enhances Electrocatalytic Performances of Alcohol Oxidations, *Angew. Chem., Int. Ed.*, 2024, **63**, e202409419.
33 F. He, Y. Zhao, X. Yang, S. Zheng, B. Yang, Z. Li, Y. Kuang, Q. Zhang, L. Lei, M. Qiu, L. Dai and Y. Hou, Metal–Organic Frameworks with Assembled Bifunctional Microreactor for Charge Modulation and Strain Generation toward Enhanced Oxygen Electrocatalysis, *ACS Nano*, 2022, **16**, 9523–9534.
34 Z. F. Huang, J. Song, Y. Du, S. Xi, S. Dou, J. M. V. Nsanzimana, C. Wang, Z. J. Xu and X. Wang, Chemical and structural origin of lattice oxygen oxidation in Co–Zn oxyhydroxide oxygen evolution electrocatalysts, *Nat. Energy*, 2019, **4**, 329–338.
35 X. Luo, H. Zhao, X. Tan, S. Lin, K. Yu, X. Mu, Z. Tao, P. Ji and S. Mu, Fe-S dually modulated adsorbate evolution and lattice oxygen compatible mechanism for water oxidation, *Nat. Commun.*, 2024, **15**, 8293.
36 F. Wang, P. Zou, Y. Zhang, W. Pan, Y. Li, L. Liang, C. Chen, H. Liu and S. Zheng, Activating lattice oxygen in high-entropy LDH for robust and durable water oxidation, *Nat. Commun.*, 2023, **14**, 6019.
37 Z. F. Huang, S. Xi, J. Song, S. Dou, X. Li, Y. Du, C. Diao, Z. J. Xu and X. Wang, Tuning of lattice oxygen reactivity and scaling relation to construct better oxygen evolution electrocatalyst, *Nat. Commun.*, 2021, **12**, 3992.